Raman Antenna Effect from Exciton-Phonon Coupling in Organic Semiconducting Nanobelts

Mao Wang[*†], *Yi Gong*[†], *Francesc Alzina*[‡], *Ondrej Svobada*[ǁ], *Belén Ballesteros*[‡], *Clivia M. Sotomayor Torres*[‡], *Senbo Xiao*[†], *Zhiliang Zhang*[†], *and Jianying He*[*†]

[†]NTNU Nanomechanical Lab, Department of Structural Engineering, Norwegian University of Science and Technology (NTNU), Trondheim, 7491, Norway

[‡]Catalan Institute of Nanoscience and Nanotechnology (ICN2), CSIC and the Barcelona Institute of Science and Technology, Campus UAB, Bellaterra, Barcelona, 08193, Spain

[ǁ]Institute of Solid Mechanics, Mechatronics and Biomechanics, Faculty of Mechanical Engineering, Brno University of Technology, Technická 2896/2, Brno, 616 69, Czech Republic

Keywords

organic semiconductor; exciton-phonon coupling; Raman antenna effect; polarized Raman spectroscopy; resonant Raman spectroscopy.

Abstract

The highly anisotropic interactions in organic semiconductors together with the soft character of organic materials lead to strong coupling between nuclear and exciton dynamics, which potentially results in anomalous electrical, optical and optoelectrical properties. Here, we report on the unprecedented Raman antenna effect from organic semiconducting nanobelts 6,13-dichloropentacene (DCP), resulting from the coupling of molecular excitons and intramolecular phonons. The highly ordered crystalline structure in DCP nanobelts enables the precise polarization-resolved spectroscopic measurement. The angle-dependent Raman spectroscopy under resonant excitation shows that all Raman modes from the skeletal vibrations of DCP molecule act like a nearly perfect dipole antenna $I_{Raman} \propto cos^4(\theta - 90)$, with almost zero (maximum) Raman scattering parallel (perpendicular) to the nanobelt's long-axis. The Raman antenna effect in DCP nanobelt is originated from the coupling between molecular skeletal vibrations and intramolecular exciton and the confinement of intermolecular excitons. It dramatically enhances the Raman polarization ratio ($\rho = I_{\parallel}/I_{\perp} > 25$) and amplifies the anisotropy of the angle-dependent Raman scattering ($\kappa_{Raman} = I_{max}/I_{min} > 12$) of DCP nanobelts. These findings have crucial implications for fundamental understanding on the exciton-phonon coupling and its effects on the optical properties of organic semiconductors.

Introduction

An antenna is a basic electrical device that receives and transmits polarized electromagnetic (EM) radiation with a dipolar dependence.[1] The Raman antenna effect was firstly reported on single-walled carbon nanotubes (SWNTs),[2] where the backscattering Raman intensity from both radial and tangential nanotube phonons exhibited the same dipole pattern $I_{Raman} \propto cos^2(\theta)$, clearly deviating from the corresponding Raman selection rule of the SWNTs. The breakdown of the predicted selection rules was attributed to depolarization effects caused by the anisotropic shape of the nanotubes and the resonance effects. However, the strongly polarized Raman scattering in highly crystalline inorganic nanowires arises from photon confinement effect dominating over the bulk Raman selection rule. When the diameter of the nanowire is small enough, the highly anisotropic geometry leads to a giant confinement of inner electric field distribution $E_{\parallel} \gg E_{\perp}$ and all the Raman modes have the strongest emission along the nanowire axis ($E_{\parallel}$ and $E_{\perp}$represents the inner electric field which is parallel or perpendicular to the nanowire axis, respectively).[3-6] To our best knowledge, the Raman antenna effect has not been reported on organic semiconducting materials so far.

Different from inorganic semiconductors, the basic units in organic small-molecule semiconductor are conjugated molecules, between which the interactions can be highly anisotropic.[7-9] When it comes to light interaction with organic semiconductor at molecular scale, each molecule acts as a basic functional unit, and the interactions between the neighboring units further tune the properties of the individual molecules. Thus, both effects contribute to the bulk optoelectrical properties of organic semiconductors.[10-12] Highly directional electronic delocalization and energy transfer in one-dimensional (1D) organic

crystalline micro/nano structures are anticipated to arise from the anisotropic interactions between neighboring molecules and give rise to anisotropic bulk optical/electrical-related properties, such as polarized photoluminescence and anisotropic carrier transport.[13-17] Moreover, the intrinsic "soft" nature of organic materials usually leads to strong coupling between the excited molecules (intramolecular excitons and intermolecular excitons) and the molecular skeletal vibrations (often referred as intramolecular phonons).[18-20] The so-called exciton–phonon coupling in organic materials play an important role in a diverse class of physical and chemical processes, ranging from heat transport at molecular junction,[18] formation and transport of polarons in organic semiconductors[19] to the selectivity in single-molecular chemistry.[21] However, despite many encouraging theoretical predictions,[19, 22-24] the experimental approach to the exciton-phonon coupling remains elusive due to the complexity of phonon and exciton behavior in organic semiconductors.[12]

In this work, we investigate the exciton-phonon coupling in 6,13-dichloropentacene (DCP) crystalline nanobelts. The introduction of chlorine groups at 6,13 position on the pentacene core disrupts the edge-to-face interaction between adjacent molecules and lead to 1D herringbone co-facial arrangement along crystallographic [100] direction in DCP crystalline nanobelts.[25, 26] Both experimental and calculated results have shown that the existence of large π–π overlap between adjacent molecules in DCP nanobelts leads to highly anisotropic carrier transport in bulk DCP crystals.[26, 27] Together with the good ambient stability as well as the easy syntheses and purification, DCP presents itself as an ideal candidate for studying the anisotropic coupling of exciton and molecular vibrations,

which is fundamentally important for understanding the interaction between light and organic semiconductors at molecular scale.

We use polarized resonant Raman spectroscopy to study the angular behavior of DCP raman signals under excitonic excitation. We find that DCP nanobelts act as a nearly perfect dipole antenna and the Raman signals from all the intramolecular phonons exhibit the same angular behavior: $I_{Raman} \propto cos^4(\theta - 90)$, where θ is the angle between the polarization direction of incident laser and the long-axis of DCP nanobelt. This Raman antenna effect is ascribed to the strong coupling from intramolecular excitons in highly crystalline DCP nanobelt that dominates over the intrinsic Raman behavior and the direction-confinement by the intermolecular exciton possessing an optical dipole moment along DCP's long-axis.

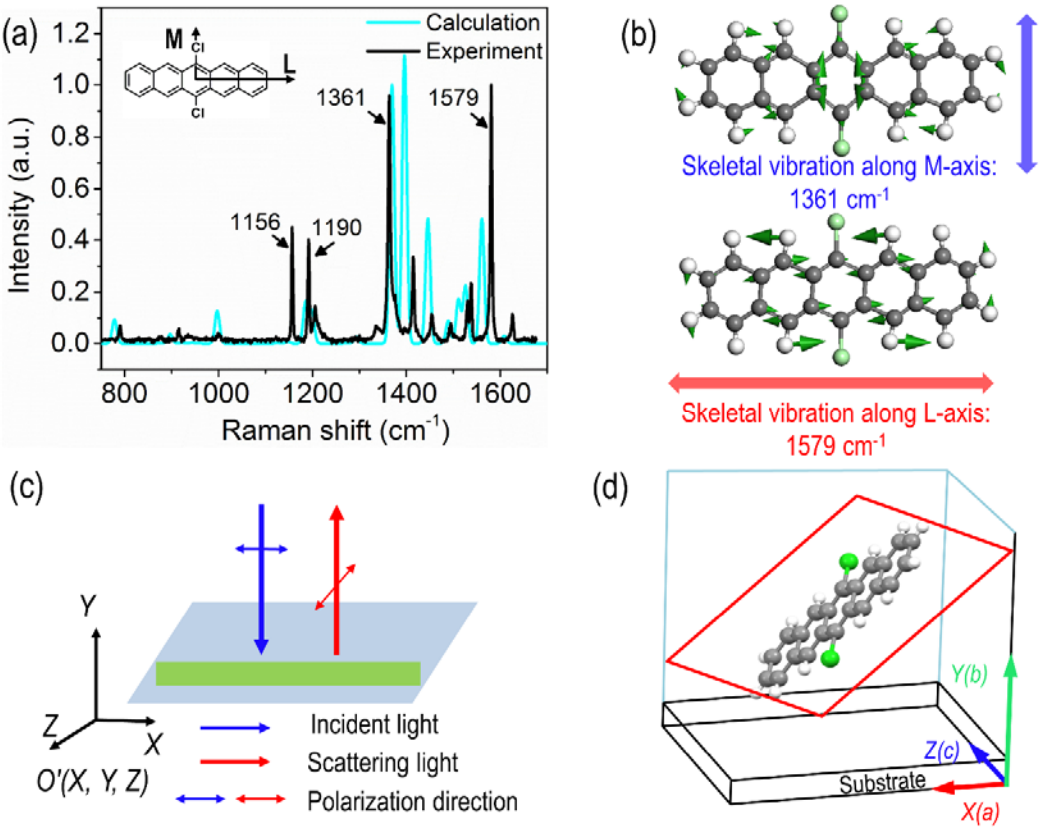

Figure 1. (a) Comparison of experimental Raman spectrum (785 nm excitation) and calculated spectrum of DCP nanobelt. The characteristic peaks are labelled. The inset figure shows the molecular structure of DCP and labelled M-axis and L-axis. (b) Schematic molecular skeletal vibrations along the short-axis (long-axis) and its corresponding Raman signals. The gray, white and green balls in the molecular structure indicate carbon, hydrogen and chlorine atoms, respectively. (c) Schematic of the experimental set-up for polarized Raman spectroscopy. The laboratory frame is indicated. (d) Plot showing the DCP molecular structure in the DCP crystalline nanobelt with respect to the substrate in the laboratory frame.

Results and Discussion

Raman Spectra of DCP.

Figure 1a shows a comparison of Raman spectra from calculation and experiments from DCP nanobelts under 785 nm excitation. We focus on the range from 750 cm^{-1} to 1650 cm^{-1} in the Raman spectra, which mainly corresponds to the skeletal C–C vibrations and the C–H bending. The calculated spectrum (no scaling factor is used) based on individual molecule agrees well at most part with the experimental results from the DCP nanobelt. The agreements between experimental and calculated vibrational frequencies allow the assignment of the observed vibrational modes in experiments. The two strongest Raman peaks at 1361 cm^{-1} and 1579 cm^{-1} from experimental spectrum correspond to the in-plane collective molecular skeletal vibrations along the short-axis (M) and long-axis (L), respectively (Figure 1b). Besides, the two peaks at 1156 cm^{-1} and 1190 cm^{-1} are assigned to the in-plane C–H bending from the ends and sides of the pentacene backbone, respectively (Figure S1). Peak 1361 cm^{-1} belongs to the totally symmetric modes (A_g), whereas 1579 cm^{-1} belongs to in-plane B_{3g} modes. These assignments are in good agreement with the previous reports on pentacene and 6,13-bis(triisopropylsilylethynyl)pentacene (TIPS-PEN) which possess the same molecular core with DCP.[28-30] These vibrations which are highly directional, can be used as indications for the molecular orientation as well as the interaction fluctuations at aggregation states.

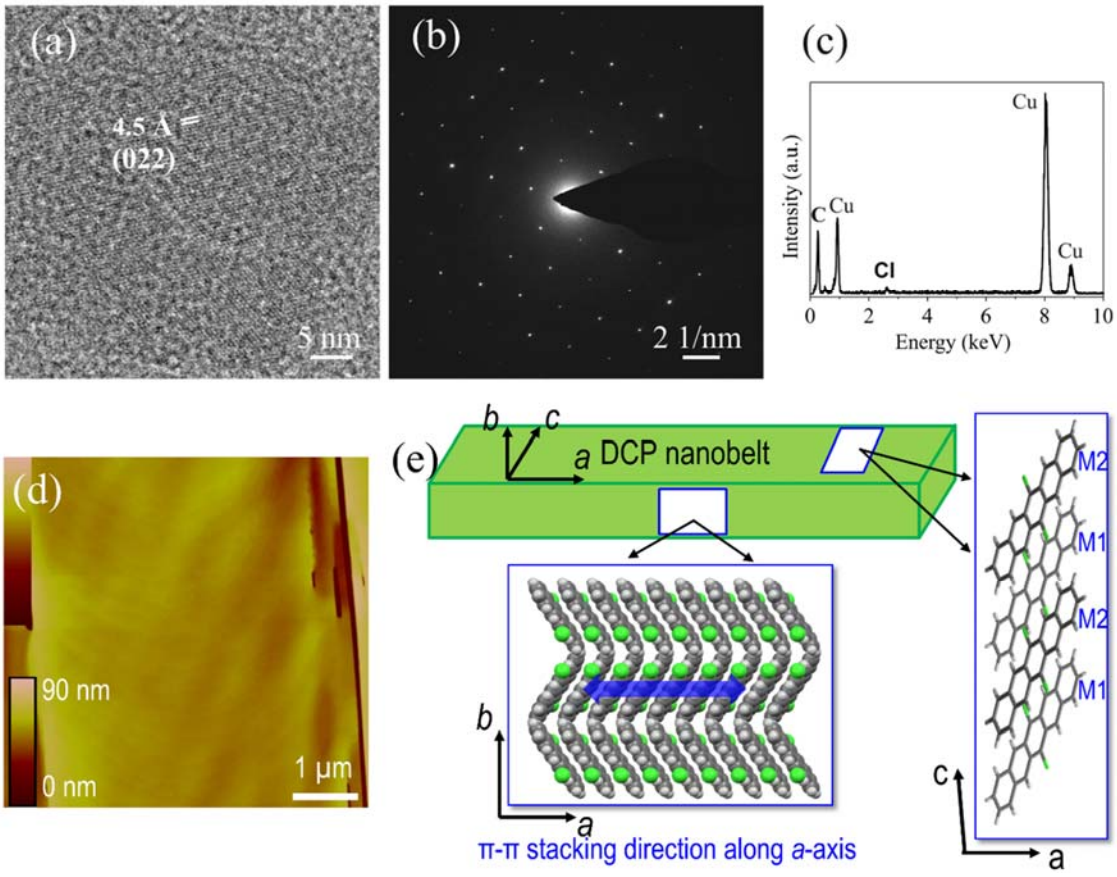

Figure 2. (a) HRTEM image of DCP nanobelt. (b) SAED pattern (along [100] zone axis) of DCP nanobelts containing an array of bright spots, indicating the single crystallinity of the nanobelts. (c) EDX analysis confirming the presence of Cl and C in the sample (Cu signal arises from the TEM grid). (d) The AFM image of the top surface of DCP nanobelt. it shows a terrace structure with layer-by-layer distance of ~9.3 ± 0.5 Å, nearly identical to half of the length of crystallographic b-axis. (e) The molecular arrangement in DCP nanobelt. Crystallographic *b*-axis is perpendicular to the substrate with π–π stacking direction along a-axis. The (*ac*)-plane is the top surface, and the two distinguishable molecules (M1 and M2) in one unit cell have the same projections on the (*ac*)-plane.

Crystalline structure of DCP nanobelt.

The optical and electrical properties of DCP crystalline nanobelt critically rely on molecular arrangement. At aggregated state, DCP molecules show strong tendency to stack along the π–π stacking direction owning to the strong face-to-face interaction between the planar cores. The single crystallinity of the DCP nanobelt is confirmed by TEM and selected area electron diffraction (SAED). The SAED pattern obtained on an individual nanobelt shows an array of bright spots (Figure 2b), which can be related to the [100] zone axis of DCP based on the single crystal data reported before.[25] The crystal structure can be further evidenced by HRTEM imaging (Figure 2a), with interplanar spacing of 4.5 Å in good agreement with the DCP (022) crystallographic plane. Additionally, Energy Dispersive X-Ray (EDX) analysis in Figure 2c of the nanobelt confirms the presence of Cl, as expected for DCP. Together with the thin-film XRD spectra (Figure S2a) which possesses two diffraction peaks corresponding to the (020) and (040) planes based on the single crystal XRD data, it is verified that DCP molecules assembled themselves in the ordered manner with *b*-axis perpendicular and (*ac*)-plane parallel to the substrate surface. The top surface of DCP nanobelt shown in the atomic force microscope (AFM) images (Figure 2d) indicates that DCP molecules grow with layer-by-layer mode and the thickness of one single layer is on average ~9.3 ± 0.5 Å, nearly identical to half of the length of crystallographic *b*-axis, which further confirms the *b*-axis is perpendicular to the substrate. A schematic of molecular arrangement in DCP nanobelt was shown in Figure 2e. The molecular arrangement viewed from two important crystallographic planes was illustrated. From (*ab*)-plane, the π–π stacking along crystallographic *a*-axis and the layered structure along *b*-axis were well showed. The top surface which is illuminated by incident light is the (*ac*)-plane. The projections on (*ac*)-plane from the two molecules (M1 and M2) in the

same unit cell exhibit the same alignment coincidently, leading to much simpler angle-dependent behavior of the Raman signals from the DCP nanobelt.

Polarized Raman Spectra of DCP Nanobelt.

Polarized Raman spectroscopy is conducted acquiring spectra with polarization which is either parallel or perpendicular to the polarization direction of incident laser.[31] The schematic of experiment method is shown in Figure 1c. The laboratory frame *O′* (*X, Y, Z*) is defined based on the frame adopted by the crystallographic structure, in which *X* direction is along crystallographic *a*-axis (the long-axis of nanobelt), *Y* direction along *b*-axis, and *Z* close to the *c*-axis (*a*-axis and *c*-axis are not orthogonal but forming an angle of 94.06°, Figure 1d). The laser is directed along the -*Y* direction and focused by the microscope objective onto *XZ*-plane. As shown in Figure 2e, the crystallographic *b*-axis of DCP nanobelt is perpendicular to the substrate and the (*ac*)-plane is the top surface on which the incident laser is focused, thus the change of polarization direction always lies in the (*ac*)-plane. During measurement, the polarization direction of the incident light was set to be perpendicular/parallel to the long-axis of the nanobelts (*X*-axis) and the scattered light was analyzed either parallel or perpendicular to incident light. Thus, four measurement configurations are adopted here: specified as $\overline{\mathrm{Y}}$(XX)Y , $\overline{\mathrm{Y}}$(XZ)Y , $\overline{\mathrm{Y}}$(ZZ)Y and $\overline{\mathrm{Y}}$(ZX)Y in Porto notation.

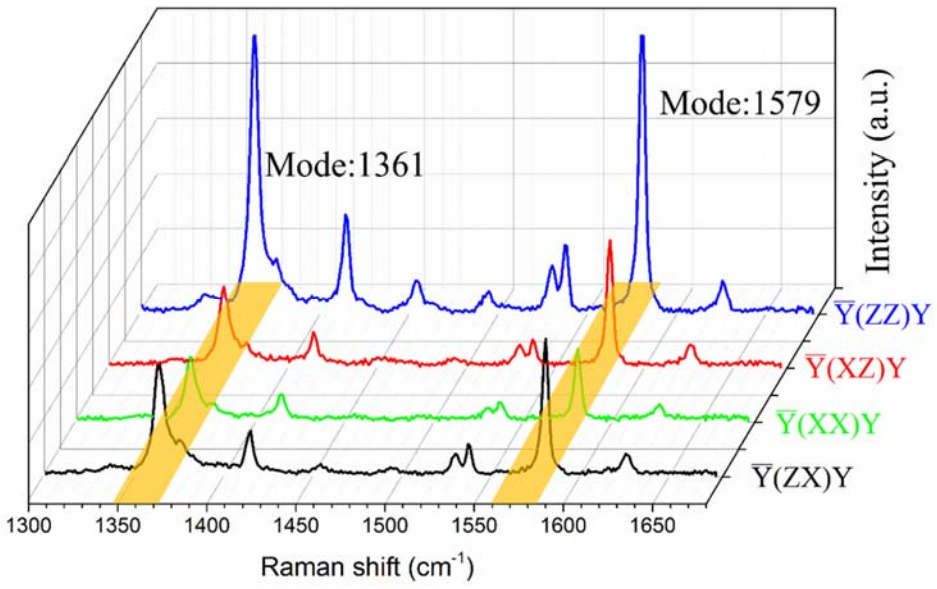

Figure 3. Polarized Raman spectra of DCP nanobelt obtained under non-resonant condition (excitation light: 785 nm) in four configurations. The two characteristic peaks (mode 1361 cm^{-1} and mode 1579 cm^{-1}) are marked. DCP nanobelt exhibits the strongest Raman signal under $\overline{Y}(ZZ)Y$ configuration.

Figure 3 shows the experimental Raman spectra in the four different configurations with the characteristic peaks at 1361 cm^{-1} and 1579 cm^{-1}. The Raman shifts of the characteristic peaks from different configurations show no apparent change, while the Raman intensities vary with experimental configurations. The polarization ratio ($\rho = I_{\parallel}/I_{\perp}$) is defined as the ratio between the parallel component ($I_{\parallel}$) and perpendicular component ($I_{\perp}$) of the Raman signal. The polarization ratios (non-resonant) when excited with light polarized along *X*- and *Z*-direction are ~0.7 and ~2.3, respectively (shown in Table 1). It indicates that the Raman signals always keep a stronger component along *Z* axis, which is perpendicular to the long-axis of the nanobelt. When comparing the two parallel configurations ($\overline{Y}(XX)Y$ and $\overline{Y}(ZZ)Y$), the Raman intensities of *Z*-polarized excitation is found to be stronger than

that of *X*-polarized excitation ($I_{\bar{Y}(ZZ)Y} / I_{\bar{Y}(XX)Y} \approx 4.1 \pm 0.2$). The anisotropic Raman scattering here is attributed merely to the anisotropic molecular stacking in the crystalline nanobelts and reflects the intrinsic Raman selection rule of DCP molecules.

Table 1. The comparison of the intensity ratios of parallel component ($I_{\parallel}$) vs. perpendicular component ($I_{\perp}$) at different excitation configurations. The error bars of the polarization ratios are based on five measurements conducted under the same conditions.

Polarization of the Excitation		$I_{\parallel}/I_{\perp}$	
		1361 cm^{-1}	1579 cm^{-1}
Z-axis	Non-resonant	2.3±0.3	2.3±0.3
	Resonant	41±3	33±2
X-axis	Non-resonant	0.8±0.1	0.6±0.1
	Resonant	0.2±0.1	1.5±0.2

The Resonant Raman Spectra of DCP Nanobelt.

To check the resonant Raman effect, a solid-state laser with wavelength of 532 nm was adopted as the excitation source given that this wavelength matches the excitonic absorption band (the absorption spectrum of DCP is shown in Figure S4, experimental details can be found in Experimental Section). The comparison of resonant and non-resonant Raman spectra is shown in Figure S5. Although the Raman shifts of all the characteristic modes show no significant changes, the Raman intensities are enormously enhanced in the resonant spectrum. The enhanced ratios of the four characteristic peaks are listed in Table 2 after correction based on the excitation power. Based on their intensity enhancement, the four characteristic peaks can be divided into three groups, which

comprise the vibrations of C–H bending (1156 cm^{-1} and 1190 cm^{-1}) showing the largest increase over 100-fold, followed by the skeletal vibrations along M-axis (1361 cm^{-1}) and L-axis (1579 cm^{-1}) with a ~91-fold and ~66-fold increase, respectively. The larger enhancements of C–H vibrations can be attributed to the low atomic weight of hydrogen atom which is more sensitive to the molecular skeletal changes on resonant excitation. For the collective vibrations of pentacene core along M-axis (1361 cm^{-1}) and L-axis (1579 cm^{-1}), the larger enhancement ratio of mode 1361 cm^{-1} indicates the stronger coupling between excitons and molecular vibrations along M-axis.

Table 2. Summary of the enhanced ratios of the four characteristic peaks under resonant excitation. The error bars of the resonant enhancement ratios are based on five measurements under the same experimental conditions.

Wavenumber (cm^{-1})	1579	1361	1190	1156
Assignment Mode	C–C ring stretch (L-axis)	C–C ring stretch (M-axis)	C–H bending (sides)	C–H bending (ends)
Resonant Enhanced Ratio	~66±3	~91±5	~114±6	~110±6

Figure 4 shows the resonant Raman spectra with different polarization configurations. All the characteristic peaks have the same Raman shift under different measurement configurations. Compared to the non-resonant Raman spectra, the most obvious feature in the resonant case is the extremely strong Raman signals under $\overline{Y}$(ZZ)Y configuration compared with that of other configurations. As shown in Table 1, the polarization ratios ($\rho = I_{\parallel}/I_{\perp}$) of resonant Raman spectra from parallel $\overline{Y}$(ZZ)Y configuration ($I_{\parallel}$) over

perpendicular $\overline{\mathrm{Y}}$(ZX)Y configuration ($I_{\perp}$) are enhanced dramatically (1361 cm^{-1}: $\rho = 41 \pm 3$ and 1579 cm^{-1}: $\rho = 33 \pm 2$). That is, the resonant effect under the *Z*-axis polarized excitation (perpendicular to the crystallographic *a*-axis) strongly polarizes the scattered Raman signals in the same polarization direction as the incident light. As for the *X*-axis polarized excitation, the Raman signals show no preferred polarization, specifically, the relative ratio of the signal from the parallel $\overline{\mathrm{Y}}$(XX)Y configuration over that of perpendicular $\overline{\mathrm{Y}}$(XZ)Y configuration is 0.2 ± 0.1 for 1361 cm^{-1} and 1.5 ± 0.2 for 1579 cm^{-1} (Table 1). It is worth noting that the resonant effect reduces the polarization ratio (ρ) for mode 1361 cm^{-1} (from 0.8 to 0.2) while increase the ratio for mode 1579 cm^{-1} (from 0.6 to 1.5). This may arise from the different coupling types (Frank-Condon type vs. vibronic coupling) between exciton and the two vibrational modes.[28]

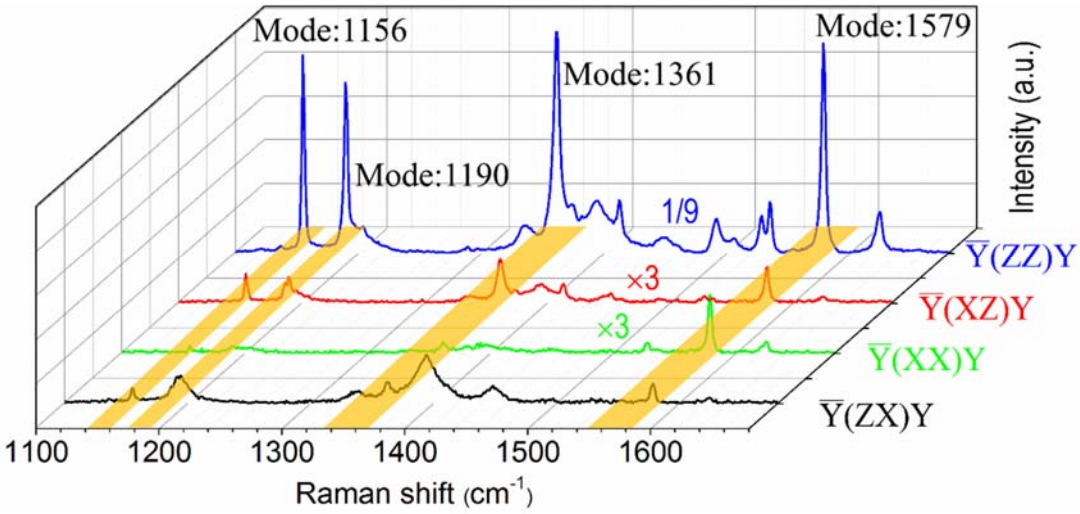

Figure 4. Polarized resonant Raman spectra obtained with four experimental configurations. The four characteristic peaks are marked. The Raman intensities are scaled by different factors for a clear comparison.

Angular Dependence of Resonant Raman Spectra of DCP Nanobelt.

(i) Raman antenna effect. To systematically investigate the anisotropic exciton-phonon coupling in DCP nanobelts, we further conducted angle-dependent Raman measurements under resonant excitation. Figure 5a shows the schematic of the experimental set-up. The polarization of the incident light (polarizer in Figure 5a) and analyzer were set to the same direction, and we changed the polarization angle (θ) by rotating the sample around the *Y*-axis. The polarization angle is set to zero when the polarization of incident light aligns with nanobelt's long-axis.

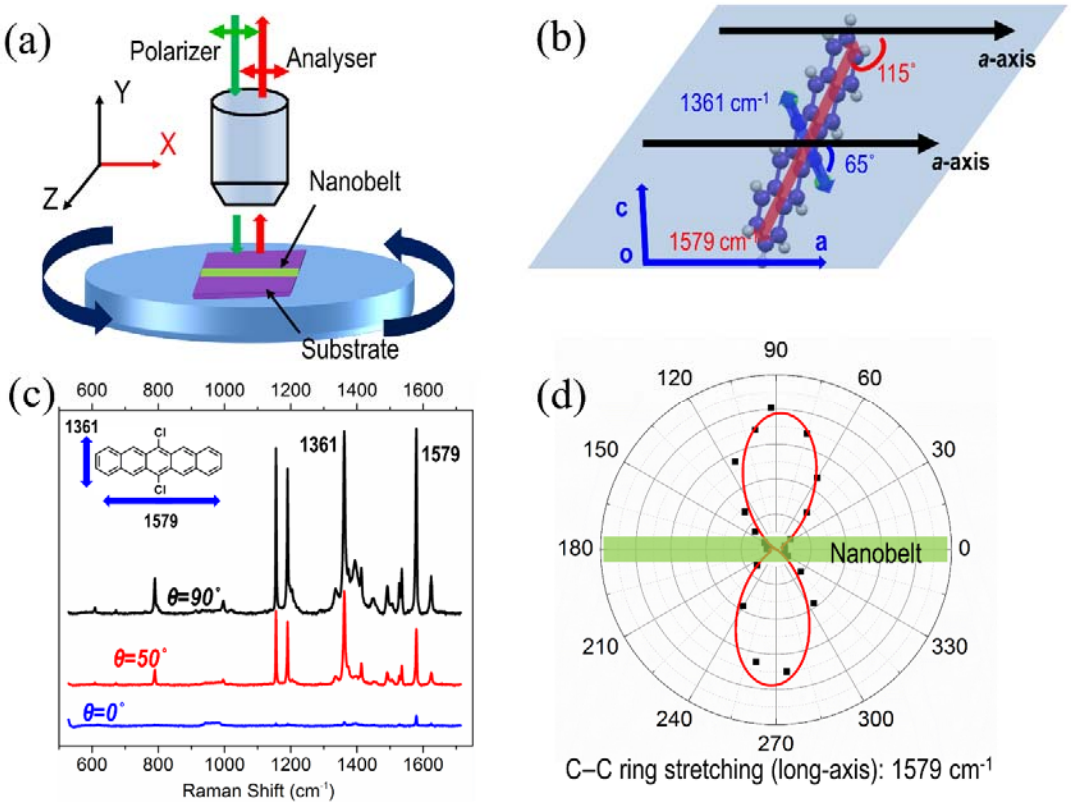

Figure 5. (a) Schematic of the experimental set-up of angle-dependent Raman spectroscopy. The sample is counter-clockwise rotated in the *XZ* plane. (b) Schematic of the projection of DCP molecule in crystallographic (*ac*)-plane. The red and blue arrows

indicate the collective skeletal vibrations along molecular long-axis (L-axis) and short-axis (M-axis), which form angles of 115° and 65° with respect to crystallographic *a*-axis, respectively. (c) Raman spectra at different polarization angles. The inset image shows the characteristic peaks related to the collective skeletal vibrations of the DCP molecule. (d) Angular dependence of the Raman intensity of peak 1579 cm^{-1}. The solid line is a fit of $I(\theta) \propto kcos^4(\theta - b)$ to the data points (b = 90 ± 4, k and b are fitting parameters). The direction of the nanobelt is indicated by the green bar.

The molecular vibrations corresponding to the characteristic Raman peaks of DCP are highly directional and their angular dependence behavior can be used as an indicator of the anisotropic coupling effects. It is worth noting that the projections on (*ac*)-plane of two molecules in the same unit cell have the same orientation, as shown in Figure 2e. Figure 5b is a schematic diagram of the projection of one DCP molecule on (*ac*)-plane with the collective displacements of the modes (1361 cm^{-1} and 1579 cm^{-1}) embedded. During the change of polarization angle in *XZ*-plane, we only consider the molecules' projections in (*ac*)-plane which form an angle of ~65° (1361 cm^{-1}) and ~115° (1579 cm^{-1}) with respect to crystallographic *a*-axis, respectively. When ignoring the resonant effects, the relevant Raman peaks are expected to maximize as the polarization of incident light aligns with its collective vibrational direction.[30, 32] This means, the signal of mode 1361 cm^{-1} reaches maximum at $\theta \approx 65°$ and mode 1579 cm^{-1} peaks at $\theta \approx 115°$ solely based on the Raman selection rule of DCP molecule. In contrast, our results from the resonant Raman spectroscopy show that the DCP nanobelt acts as a nearly perfect "Raman antenna" and all the Raman signals possess the same behavior and reach the strongest intensity when $\theta \approx 90°$, and weakest when $\theta \approx 0°$ (Figure 5c, 5d and Figure S6). The Raman intensity

anisotropy of all peaks ($\kappa_{Raman} = I_{90}/I_0$), is largely enhanced compared to the anisotropy of the Raman spectra under the non-resonant condition (shown in Table 3). The enhanced anisotropy of peak 1361 cm^{-1} (26-fold) is stronger than that of peak 1579 cm^{-1} (12-fold) further verifying the stronger coupling strength between optical exciton and the vibrations along the DCP short-axis.

Table 3. The comparison of Raman intensity anisotropy ($\kappa_{Raman} = I_{90}/I_0$) of DCP nanobelts under non-resonant and resonant excitation. The error bars of the ratio in the table are based on five measurements under the same condition.

	κ_{Raman}			
Excitation	1156 cm^{-1}	1190 cm^{-1}	1361 cm^{-1}	1579 cm^{-1}
Non-resonant	3.0±0.5	3.4±0.5	4.0±0.5	4.2±0.5
Resonant	28.2±4	23.1±3	26.0±5	12.2±3

To understand the anomalous angular Raman behavior of DCP nanobelt, we need to consider the excitons in DCP nanobelts and their effects on molecular skeletal vibrations. As DCP has a similar chromophore to pentacene, the optical transition dipole moment of DCP aligns with the molecular short-axis.[27, 33, 34] That is, the optical transition dipole moment of DCP has the same direction as the collective vibrations along M-axis, and forms an angle of ~65° with *X*-axis (the long-axis of nanobelt). Therefore, the intramolecular exciton–phonon coupling is stronger along the M-axis and leads to larger resonant effects for the 1361 cm^{-1} mode. Additionally, the associated vibrational energy deduced from the energy spacing between vibronic bands in the absorption spectrum of DCP is ~1333 cm^{-1} (Figure S4). This value is reasonably close to the energy of the skeletal vibrations along

the M-axis, which further supports a stronger intramolecular exciton–phonon coupling in this direction. DCP forms both intramolecular and intermolecular excitons, among which the latter has an optical transition dipole moment oriented along the direction of π-π stacking (the same direction of DCP nanobelt's long-axis).[35, 36] The formation of intermolecular exciton attenuates the *X*-axis component of the incident light, because intermolecular excitons which delocalize over several molecules have weak contribution to the resonant enhancement of the intramolecular phonons. Therefore, the selection rule of resonant effect is expected to align with *Z* direction, that is, perpendicular to the long-axis of nanobelt. With the rotation of sample, the Raman signals of DCP follow nearly as $I_{Raman} \propto cos^4(\theta - 90)$. The fitted curve is shown in Figure 5d and Figure S6. The fitting contour captures the main characteristics of the resonant polarized Raman: all the Raman peaks possess the same angle-dependent behavior and the Raman signals reach maximum at $\theta \approx 90°$ and minimum at $\theta \approx 0°$, respectively. As the Raman antenna behavior arises from the combined effects of both intramolecular and intermolecular excitons, it is expected that the results also apply to other organic semiconducting systems with close 1D π-π stacking that leads to the formation of delocalized electronic state. It is worth noting that the Raman signals follow a quartic cosine function instead of the quadratic one reported in some other reports.[36] It is caused by the difference between the experimental set-up. In the report of James, D. T. et al. and coauthors, only the polarization of incident light was changed in their experiments while the orientation of the sample was fixed, and the detected Raman signals are not polarization-distinguished. In this case, the quadratic cosine pattern was obtained. In our experiment, the polarization of polarizer and analyzer are fixed while

rotating the sample, thus both the polarization-dependence of incident and scattered light are included and it leads to the cosine function raised to the fourth power.

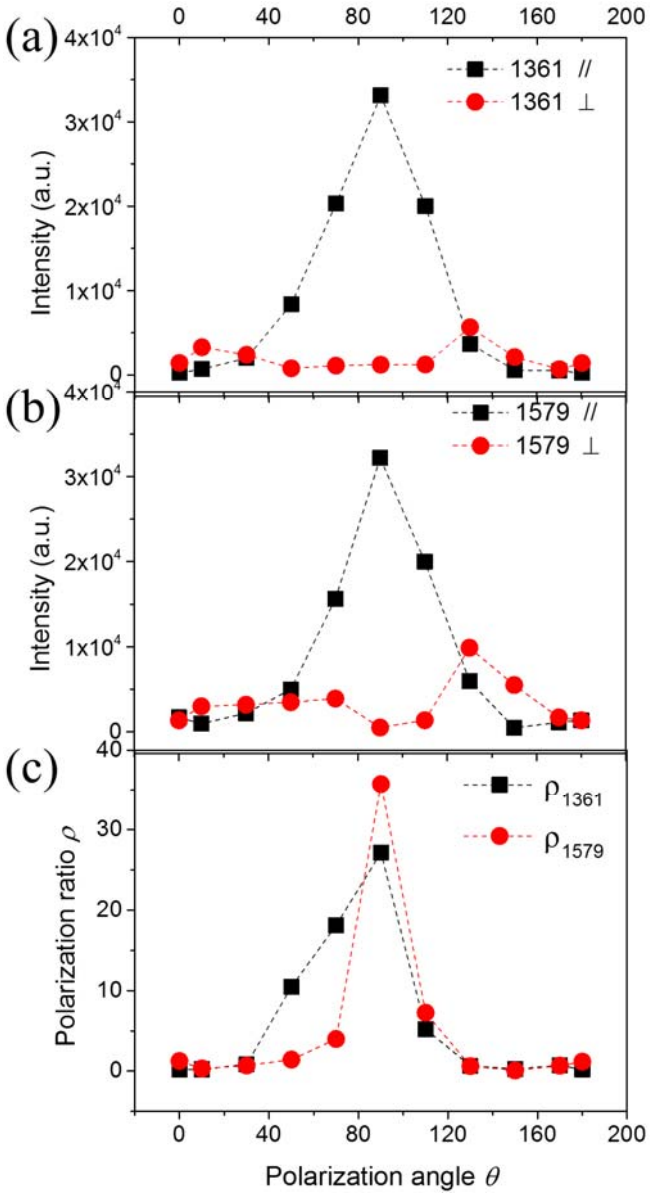

Figure 6. The parallel and perpendicular components of the Raman signal of (a) 1361 cm^{-1} and (b) 1579 cm^{-1} at different polarization angles. (c) The polarization ratio ($\rho = I_{\parallel}/I_{\perp}$) of peak 1361 cm^{-1} and 1579 cm^{-1} at different polarization angles.

(ii) The analysis of polarization components of Resonant Raman spectra. To further investigate the coupling of exciton and phonon in DCP nanobelt, we analyze the polarized components ($I_{\parallel}$ and $I_{\perp}$) of the Raman signals at each polarization angle under resonant condition. The polarization direction of incident light is fixed, and the parallel $I_{\parallel}$ and perpendicular $I_{\perp}$ components (compared to the incident laser) are checked at each rotating angle (Figure 6a and 6b). Mode 1361 cm^{-1} and 1579 cm^{-1} are selected as the representative peaks. Although corresponding to different vibration patterns, the components from both modes show similar angular dependence as the sample rotates. Whereas the $I_{\parallel}$ follows the quartic pattern of resonant effects ($I_{\parallel} \propto \cos^4(\theta - 90)$), the angle-dependent pattern of the perpendicular components $I_{\perp}$ is not that clear. The angular dependence of $I_{\perp}$ here reflects the interplay between resonant enhancement and the intrinsic Raman selection rule. Although a quantitative analysis requires the accurate values of the Raman tensor under the resonant condition, it is still instructive to qualitatively analyze the angular behavior of the Raman signals. At $\theta = 0°$, the total intensity of Raman signal is the lowest because of the weakest resonant effect. The parallel component $I_{\parallel}$ has the same direction with the *X*-axis (crystallographic *a*-axis), and the perpendicular components $I_{\perp}$ aligns with the *Z*-axis ($I_{\perp}$is large than $I_{\parallel}$ at non-resonant excitation). Therefore, $I_{\perp}$ has a larger relative intensity compared to $I_{\parallel}$ (polarization ratio $\rho = I_{\parallel}/I_{\perp} > 1$). As θ increases, the projection of *c*-axis on laser polarization direction increases and the Raman intensities of all modes enhance dramatically, moreover, the $I_{\parallel}$ component gradually dominates the Raman signal leading the increasing of polarization ratio (Figure 6c). At $\theta \approx 90°$, crystallographic *c*-axis aligns nearly with the polarization direction of incident light, all the modes have the strongest enhancement. The $I_{\perp}$ components are extremely weak and the polarization ratio reaches its

maximum. The scattered Raman signals are strongly polarized. With the continuing increase of polarization angle, the proportion of $I_{\perp}$ component starts to rise while the total Raman intensity decreases. At $\theta \approx 130°$, intensity of the $I_{\perp}$ component is nearly same as that of $I_{\parallel}$ component. In general, the perpendicular component shows a combined effect from the intrinsic DCP Raman selection rule and the resonant effects, whereas the resonant effects dominate over the molecular Raman selection rule on the trend of overall intensities and the parallel component.

Conclusion

We have investigated the exciton-phonon coupling of a model organic semiconductor – 6,13-dichloropentacene (DCP) crystalline nanobelt by polarized Raman spectroscopy under non-resonant and resonant excitation. A certain degree of anisotropy of the non-resonant Raman spectra of DCP nanobelt is observed and attributed to the anisotropic molecular arrangement in the crystalline structure. Under resonant excitation, strong enhancement (> 66-fold) of the Raman signals indicates strong coupling of exciton and intramolecular phonons in DCP nanobelts. More importantly, DCP nanobelts are found to act as a nearly perfect Raman antenna and the angular dependence of all the Raman signals from different intramolecular phonons exhibits a simple $cos^4(\theta - 90)$ pattern. Strongest (weakest) Raman scattering is obtained when the polarization direction of incident laser is perpendicular (parallel) to the long axis of nanobelts. The Raman signals from all the vibration modes are highly polarized with a polarization ratio ($\rho = I_{\parallel}/I_{\perp}$) over 25 at the perpendicular excitation. This Raman antenna effect is attributed to the strong molecular exciton-phonon coupling in DCP nanobelts under resonant excitation that dominates over

the intrinsic Raman selection rule and lead all the Raman modes behave the same. The formation of intermolecular excitons in DCP nanobelt further confine the maximum Raman signals at the perpendicular direction relative to the long axis of DCP nanobelt. Besides the enhanced Raman intensity from the coupling effect, the anisotropy of the Raman scattering ($\kappa_{Raman} = I_{90} / I_0$) from DCP nanobelts is strongly amplified (for 1579 cm^{-1}: $\kappa_{Raman} > 12$, for 1361 cm^{-1}: $\kappa_{Raman} > 20$). Our results demonstrate DCP's potential as the active materials for multifunctional optoelectronics for polarized light, such as organic detectors, switches, antenna, etc. Furthermore, these findings are expected to apply to other organic semiconducting materials which possess herringbone 1D π-π stacking and enrich our knowledge on the light-matter interaction in organic semiconducting systems.

Experimental Section

Preparation and Characterization of DCP Nanobelts.

6,13-dichloropentacene (DCP) was synthesized following the same process as previous report.[25] Two kinds of DCP nanobelts with different thicknesses were characterized by Raman spectroscopy. Two different groups of DCP nanobelts were measured. The thin DCP nanobelt (thickness between 40 to 80 nm, width of 4 to 6 μm and length of several hundreds of micrometers) served as the sample for resonant Raman measurement. For the non-resonant Raman experiment, we used the thick nanobelts (thickness between 0.8 to 3 μm, width of 0.2 to 6 μm and length of several hundreds of micrometers) to ensure enough signals under all the different experimental configurations. For thick nanobelts, ~1.0 mg/mL solution of DCP in toluene was dropcast onto octadecyltrimethoxysilane (OTS)-modified SiO_2/Si on top of a hotplate held at ~85 °C. After deposition, the substrates were

covered with a Petri dish to control solvent evaporation. Within 5 minutes, random-aligned nanobelts formed, and the samples were annealed subsequently at 100 °C for another 5 min to remove the residual solvent. The preparation method of the thin nanobelt arrays was reported in our previous report.[35] Briefly, ~1.0 mg/mL solution of DCP in *o*-dichlorobenzene was dropcast onto plasma-treated silicon substrate on top of a hotplate held at ~140 °C, a piece of silicon wafer was used as the pinner to steady the receding line. After solvent evaporation, large-area well-aligned DCP nanobelt arrays were formed with controlled growth direction, followed by a similar annealing procedure at 150 °C. The optical microscope images of the two different DCP nanobelts were shown in Figure S2 and Figure S3. The surface morphology was investigated with AFM (Veeco) under ambient condition. Transmission electron microscopy (TEM) images and selected area electron diffraction (SAED) patterns were acquired using an FEI Tecnai G2 F20 HRTEM operated at 80 kV to minimize beam damage on the samples. TEM samples were prepared by peeling off the organic layer from the Si wafer with a scraper blade. The obtained segments of DCP nanobelt were dispersed in ethanol and were then deposited on a carbon coated Cu TEM grid. Energy Dispersive X-Ray (EDX) spectra were obtained with an EDAX super ultra-thin window (SUTW) X-ray detector.

Raman Characterization.

The Renishaw InVia Reflex Spectrometer System was the main instrument for all the Raman-related measurements. For non-resonant Raman characterization, the excitation laser was 785 nm. The output intensity of the laser was set to be 3 mW (1×3s exposure time) for all the non-resonant measurement on thick DCP nanobelts. For resonant Raman experiment, a 532 nm solid-state laser was used as the excitation source. The output intensity was 5 mW (1×5s exposure time). A half-wave and a quarter-wave plate (polarizer)

were inserted between the laser source and samples to adjust the polarization of incident laser. The laser spot was focused on the samples through a 50× objective (Numerical Aperture: 0.75) with a spot diameter of ~2 μm. The polarized Raman spectra were obtained in the back-scattering configuration by adding another set of half-wave and polarizer (analyzer) mounted before the CCD to adjust the polarization of Raman signals. The Raman signals exhibited nearly identical intensities for repeated measurement at the same site on DCP nanobelt, so we kept the same position under the illumination after each rotation, the error bars of the polarization ratios and resonant enhancement ratios in the main text were based on five measurements under the same condition. All measurements were conducted under ambient conditions. To make sure the reproducibility of the resonant Raman characterization, the angle-dependent Raman measurements were conducted on the HORIBA T64000 Spectrometer System with a liquid-nitrogen cooled CCD detector. A rotatable half-wave plate was inserted between the laser source and samples to adjust the polarization of incident light to the desired angle in the horizontal plane. The Raman signals from the sample were collected by the objective lens (50× and Numerical Aperture: 0.55) with backscattering mode and then passed again through the same half-wave plate where the polarization was counter-rotated by the same angle. The light intensity on the sample surface was kept lower than 0.7 mW (checked by a photodiode) to avoid potential sample damage. The measurement configuration was equivalent to that on the Renishaw InVia Reflex Spectrometer System with rotating the sample while keeping the polarizer and analyzer fixed. The Raman signals also exhibited the same quartic pattern ($\cos^4(\theta-90)$) in which maximum signal was obtained at the polarization angle of ~90°.

Vibrational Analysis of the Raman Spectra.

Density functional perturbation theory (DFPT) was adopted to analyze the molecular vibrational properties of DCP for interpreting the Raman spectrum.[37] The calculation was performed using the Vienna Ab initio Simulation package (VASP).[38] In order to obtain the Raman spectrum of an isolated DCP molecule, a "molecule in a box" system was built. DCP molecule was placed in a large vacuum periodic box (with dimension a: 30Å, b: 30 Å and c: 30Å, α=β=γ=90˚) in the system, mimicking a non-interacting supercell. Such large box dimension was chosen for eliminating any possible non-bonded force effect from adjacent molecules. The generalized gradient approximations (GGA) using the exchange-correlation functional proposed by Perdew, Burke, and Ernzerhof (PBE) was adopted to combine with a plane-wave basis set in the calculation.[39] The selection of K-point was the Gamma point only. The energy cutoff for electronic was 850.0 eV. After convergence test, the relaxed molecular structure was directly used for probing the frequencies of all vibrational modes without using any symmetry. Specifically, differences in energy with and without atomic displacement in each vibrational mode were collected at individual displacement step. The second derivative constant of the energy on the displacement step size (force constant) was then used for deducing vibrational frequency utilizing a harmonic oscillator model.

ASSOCIATED CONTENT

Supporting Information. The atomic displacements of different Raman modes based on DFPT calculations. Detailed information on the crystalline structure of DCP nanobelts. Surface morphology (AFM images) of DCP nanobelt. The absorption spectra of DCP solution and nanobelts. The comparison of the non-resonant and resonant Raman spectra

of DCP nanobelt. The angular dependence of other characteristic Raman signals and the corresponding molecular displacement diagrams.

AUTHOR INFORMATION

Corresponding Author

*Email: mao.wang@ntnu.no; jianying.he@ntnu.no

Notes

The authors declare no competing financial interest.

ACKNOWLEDGMENT

This work is financially supported by NTNU, The Research Council of Norway, Det Norske Oljeselskap ASA and Wintershall Norge AS via WINPA project (Grant No. NANO2021 and PETROMAKS2 234626). The Research Council of Norway is acknowledged for the support to the Norwegian Micro- and Nano-Fabrication Facility, NorFab (197411). Computational resources were provided by Norwegian Metacenter for Computational Science (NOTUR and NN9391k), the CESNET LM2015042 and the CERIT Scientific Cloud LM2015085, provided under the program "Projects of Large Research, Development, and Innovations Infrastructures". ICN2 is supported by the Severo Ochoa program from Spanish MINECO (Grant No. SEV-2013-0295).

Reference

1. Stutzman, W. L.; Thiele, G. A. *Antenna theory and design*. John Wiley & Sons: 2012.
2. Duesberg, G. S.; Loa, I.; Burghard, M.; Syassen, K.; Roth, S. Polarized Raman Spectroscopy on Isolated Single-Wall Carbon Nanotubes. *Phys Rev Lett* 2000, 85, 5436-5439.

3. Wu, J.; Zhang, D.; Lu, Q.; Gutierrez, H. R.; Eklund, P. C. Polarized Raman scattering from single GaP nanowires. *Physical Review B* 2010, 81, 165415.
4. Chen, G.; Wu, J.; Lu, Q.; Gutierrez, H. R.; Xiong, Q.; Pellen, M. E.; Petko, J. S.; Werner, D. H.; Eklund, P. C. Optical Antenna Effect in Semiconducting Nanowires. *Nano Lett* 2008, 8, 1341-1346.
5. Lopez, F. J.; Hyun, J. K.; Givan, U.; Kim, I. S.; Holsteen, A. L.; Lauhon, L. J. Diameter and Polarization-Dependent Raman Scattering Intensities of Semiconductor Nanowires. *Nano Lett* 2012, 12, 2266-2271.
6. Möller, M.; de Lima, M. M.; Cantarero, A.; Dacal, L. C. O.; Madureira, J. R.; Iikawa, F.; Chiaramonte, T.; Cotta, M. A. Polarized and resonant Raman spectroscopy on single InAs nanowires. *Physical Review B* 2011, 84, 085318.
7. Coropceanu, V.; Cornil, J.; da Silva Filho, D. A.; Olivier, Y.; Silbey, R.; Brédas, J.-L. Charge Transport in Organic Semiconductors. *Chem Rev* 2007, 107, 926-952.
8. Allard, S.; Forster, M.; Souharce, B.; Thiem, H.; Scherf, U. Organic Semiconductors for Solution-Processable Field-Effect Transistors (OFETs). *Angew Chem Int Ed* 2008, 47, 4070-4098.
9. Mas-Torrent, M.; Rovira, C. Role of Molecular Order and Solid-State Structure in Organic Field-Effect Transistors. *Chem Rev* 2011, 111, 4833-4856.
10. Scholes, G. D.; Rumbles, G. Excitons in nanoscale systems. *Nat Mater* 2006, 5, 683-696.
11. Fraboni, B.; Fraleoni-Morgera, A.; Geerts, Y.; Morpurgo, A.; Podzorov, V. Organic Single Crystals: An Essential Step to New Physics and Higher Performances of Optoelectronic Devices. *Adv Funct Mater* 2016, 26, 2229-2232.
12. Ostroverkhova, O. Organic Optoelectronic Materials: Mechanisms and Applications. *Chem Rev* 2016, 116.
13. Kim, F. S.; Ren, G.; Jenekhe, S. A. One-Dimensional Nanostructures of π-Conjugated Molecular Systems: Assembly, Properties, and Applications from Photovoltaics, Sensors, and Nanophotonics to Nanoelectronics. *Chem Mater* 2011, 23, 682-732.
14. Minari, T.; Liu, C.; Kano, M.; Tsukagoshi, K. Controlled Self-Assembly of Organic Semiconductors for Solution-Based Fabrication of Organic Field-Effect Transistors. *Adv Mater* 2012, 24, 299-306.
15. Garcia-Frutos, E. M. Small organic single-crystalline one-dimensional micro- and nanostructures for miniaturized devices. *Journal of Materials Chemistry C* 2013, 1, 3633-3645.
16. Min, S.-Y.; Kim, T.-S.; Lee, Y.; Cho, H.; Xu, W.; Lee, T.-W. Organic Nanowire Fabrication and Device Applications. *Small* 2015, 11, 45-62.
17. Um, H. A.; Lee, D. H.; Heo, D. U.; Yang, D. S.; Shin, J.; Baik, H.; Cho, M. J.; Choi, D. H. High Aspect Ratio Conjugated Polymer Nanowires for High Performance Field-Effect Transistors and Phototransistors. *ACS Nano* 2015, 9, 5264-5274.
18. Ward, D. R.; Corley, D. A.; Tour, J. M.; Natelson, D. Vibrational and electronic heating in nanoscale junctions. *Nat Nanotech.* 2011, 6, 33-38.
19. Tamura, H.; Tsukada, M.; Ishii, H.; Kobayashi, N.; Hirose, K. Roles of intramolecular and intermolecular electron-phonon coupling on the formation and transport of large polarons in organic semiconductors. *Physical Review B* 2012, 86, 035208.
20. Bakulin, A. A.; Lovrincic, R.; Yu, X.; Selig, O.; Bakker, H. J.; Rezus, Y. L.; Nayak, P. K.; Fonari, A.; Coropceanu, V.; Bredas, J. L.; Cahen, D. Mode-selective vibrational modulation of charge transport in organic electronic devices. *Nat Commun* 2015, 6, 7880-7887.
21. Pascual, J. I.; Lorente, N.; Song, Z.; Conrad, H.; Rust, H. P. Selectivity in vibrationally mediated single-molecule chemistry. *Nature* 2003, 423, 525-528.
22. Hennessy, M. H.; Soos, Z. G.; Pascal Jr, R. A.; Girlando, A. Vibronic structure of PTCDA stacks: the exciton–phonon-charge-transfer dimer. *Chem Phys* 1999, 245, 199-212.

23. Spano, F. C. The Spectral Signatures of Frenkel Polarons in H- and J-Aggregates. *Acc Chem Res* 2010, 43, 429-439.
24. Cui, Y.; Lauchner, A.; Manjavacas, A.; García de Abajo, F. J.; Halas, N. J.; Nordlander, P. Molecular Plasmon–Phonon Coupling. *Nano Lett* 2016, 16, 6390-6395.
25. Li, J.; Wang, M.; Ren, S.; Gao, X.; Hong, W.; Li, H.; Zhu, D. High performance organic thin film transistor based on pentacene derivative: 6,13-dichloropentacene. *J Mater Chem* 2012, 22, 10496-10500.
26. Wang, M.; Li, J.; Zhao, G.; Wu, Q.; Huang, Y.; Hu, W.; Gao, X.; Li, H.; Zhu, D. High-Performance Organic Field-Effect Transistors Based on Single and Large-Area Aligned Crystalline Microribbons of 6,13-Dichloropentacene. *Adv Mater* 2013, 25, 2229-2233.
27. Zhang, X.; Yang, X.; Geng, H.; Nan, G.; Sun, X.; Xi, J.; Xu, X. Theoretical comparative studies on transport properties of pentacene, pentathienoacene, and 6,13-dichloropentacene. *J Comput Chem* 2015, 36, 891-900.
28. Yamakita, Y.; Kimura, J.; Ohno, K. Molecular vibrations of [n]oligoacenes (n=2−5 and 10) and phonon dispersion relations of polyacene. *The Journal of Chemical Physics* 2007, 126, 064904.
29. Hosoi, Y.; Deyra, D. M.; Nakajima, K.; Furukawa, Y. Micro-Raman Spectroscopy on Pentacene Thin-Film Transistors. *Molecular Crystals and Liquid Crystals* 2008, 491, 317-323.
30. James, D. T.; Kjellander, B. K. C.; Smaal, W. T. T.; Gelinck, G. H.; Combe, C.; McCulloch, I.; Wilson, R.; Burroughes, J. H.; Bradley, D. D. C.; Kim, J.-S. Thin-Film Morphology of Inkjet-Printed Single-Droplet Organic Transistors Using Polarized Raman Spectroscopy: Effect of Blending TIPS-Pentacene with Insulating Polymer. *ACS Nano* 2011, 5, 9824-9835.
31. Tanaka, M.; Young, R. J. Review Polarised Raman spectroscopy for the study of molecular orientation distributions in polymers. *Journal of Materials Science* 2006, 41, 963-991.
32. Sebastian, W.; Joseph Razzell, H.; Ji-Seon, K. Raman spectroscopy as an advanced structural nanoprobe for conjugated molecular semiconductors. *J Phys D: Appl Phys* 2017, 50, 073001.
33. Tiago, M. L.; Northrup, J. E.; Louie, S. G. Ab initio. *Physical Review B* 2003, 67, 115212.
34. Wong, C. Y.; Cotts, B. L.; Wu, H.; Ginsberg, N. S. Exciton dynamics reveal aggregates with intermolecular order at hidden interfaces in solution-cast organic semiconducting films. *Nat Commun* 2015, 6, 5946-5952.
35. Wang, M.; Gong, Y.; Alzina, F.; Sotomayor Torres, C. M.; Li, H.; Zhang, Z.; He, J. Angle-Dependent Photoluminescence Spectroscopy of Solution-Processed Organic Semiconducting Nanobelts. *The Journal of Physical Chemistry C* 2017, 121, 12441-12446.
36. James, D. T.; Frost, J. M.; Wade, J.; Nelson, J.; Kim, J.-S. Controlling Microstructure of Pentacene Derivatives by Solution Processing: Impact of Structural Anisotropy on Optoelectronic Properties. *ACS Nano* 2013, 7, 7983-7991.
37. Giannozzi, P.; Baroni, S. Vibrational and dielectric properties of C60 from density‐functional perturbation theory. *The Journal of Chemical Physics* 1994, 100, 8537-8539.
38. Kresse, G.; Hafner, J. Ab initio molecular dynamics for liquid metals. *Physical Review B* 1993, 47, 558-561.
39. Perdew, J. P.; Burke, K.; Ernzerhof, M. Generalized Gradient Approximation Made Simple. *Phys Rev Lett* 1996, 77, 3865-3868.

For Table of Contents Only